# Residual Stresses in Environmental and Thermal Barrier Coatings on Curved Superalloy Substrates: Experimental Measurements and Modelling

**D. Liu[1], S.T. Kyaw[2], P. E. J. Flewitt[1,3], M. Seraffon[4,6], N. J. Simms[4], M. Pavier[5] and I. A. Jones[2*]**

[1]Interface Analysis Centre, School of Physics, University of Bristol, Bristol, BS8 1TL, UK

[2]Division of Materials, Mechanics and Structures, University of Nottingham, University Park, Nottingham NG7 2RD, UK.

[3]HH Wills Physics Laboratory, School of Physics, University of Bristol, Bristol, BS8 1TL, UK

[4]Cranfield University, Cranfield, Bedford MK43 0AL, UK

[5]Department of Mechanical Engineering, University of Bristol, Bristol BS8 1TR, UK

[6]National Physical Laboratory, Hampton Road, Teddington TW11 0LW, UK

*Corresponding author. Tel. +44 115 951 3784 E-mail address: arthur.jones@nottingham.ac.uk (I. A. Jones)

## Abstract

Residual stresses within thermal barrier coated (TBC) systems are predicted using finite element models and are compared against experimental measurements taken using Raman and photo-stimulated luminescence piezo-spectroscopic methods. Two types of specimens were considered: flat specimens without TBC, and aerofoil shaped specimens with TBC. Comparisons between model predictions and experimentally measured stresses and also the relationship between substrate curvature and residual stresses on subsequent spallation of the aerofoil specimen were made. For the flat specimen, predicted and measured residual stresses are of the same order of magnitude. Both studies have indicated that larger compressive residual stresses arise from higher substrate curvatures. The results improve the understanding of initiation and propagation of TBC cracks which occurs preferentially at locations with high substrate convex curvature.

## 1. Introduction

Turbine blades used for land-based gas turbine power plants and aero engines operate at gas temperatures above which the parent superalloy cannot retain its integrity without additional internal cooling [1, 2]. To reduce oxidation and to further promote efficiency by operation at a higher temperature, turbine blades with ceramic thermal barrier coating systems (TBCs) were introduced into service during the early 1970s [3]. A conventional TBC system is made up of multiple layers, namley a top layer of yttria (6-8 wt.%) stabilised

zirconia (YSZ), a metallic bond coat (BC) that provides bonding between the metallic substrate and YSZ, and a thermally grown oxide (TGO) layer that forms between the TBC and BC during thermal exposure [4]. These coatings can be applied by various processes including air plasma spraying (APS) and electron beam physical vapour deposition (EBPVD) [5]. The resulting microstructure for these coating is complex and indeed there are various proportions of porosity and flaws within the final product that can modify the failure of the coating system [6-13].

The low thermal conductivity of the TBC layer allows coated components to operate at higher temperatures than the limit imposed by the underlying parent metals. Therefore it is crucial for the layers to remain attached to the components for the required service life while experiencing residual stresses during thermal cycling [6, 14]. The residual stresses within the TBC system arise from three main sources: (i) the coating deposition process [7, 15], (ii) mismatch stress upon cooling due to the differences in the thermal expansion coefficient of individual layers [6, 16] and (iii) growth of TGO adjacent to the bond coat. Tensile out-of-plane stresses within the TBC potentially cause opening of flaws and discontinuities within the coating during steady state. Furthermore, tensile out-of-plane stresses at the TBC/BC/TGO interfaces cause delamination cracks and subsequent premature failure of the TBC [17]. Therefore, residual stresses within the multilayers greatly influence the durability of the coating system and hence are worthy of investigation. Moreover, the geometry of both the substrate [18, 19] and the coating interfaces [20] can have a significant impact on stress distributions. And it has been long recognised that the TBC system fails preferentially at regions of high substrate curvature, but no systematic theoretical analysis considering the effect of residual stress has been undertaken to assist the understanding of this scenario [21].

Various researchers in recent decades have carried out stress analysis because of the importance of understanding the stress distribution within TBC systems for predicting the service life of the coatings [22-24]. FEA is one of the most popular techniques for stress analysis since the technique is cost effective, and can consider a wide variety of phenomena affecting the mechanical response of the TBC. However, due to the complex nature of the TBC systems, the reliability of the results depends critically upon the various assumptions made regarding the geometry and thickness of the coating interface and the physical and mechanical properties of the individual constitutions of the coatings etc.. While these various assumptions have been implemented within the FE models by researchers to model TBC stress distributions as realistically as possible, comparisons of simulated results against stresses measured using independent methods have remained scarce.

The current paper in turn examines the development of residual stresses in flat and curved coated superalloy specimens both analytically and numerically (FE) using a number of models. In addition, residual stresses were measured experimentally for comparison [25-27]. The study allows the phenomena explored in the theoretical models to be examined, both in terms of the stresses measured using Raman spectroscopy (RS), and in terms of the failure modes (spallation of the TBC and delamination at the coating interfaces) which result. It is worth noting that this contribution is a second stage theoretical mechanistic exploration of the role of substrate curvature on the micro- and macro-scale failure of the TBC system after the oxidation mechanisms and interfacial roughness/bonding characterisation described in a previous work [28] with the aim of incorporating the important experimental observations into a validated FEA model for future guidance in integrity evaluation and lifetime prediction of practical TBC systems on curved components.

## 2. Experiment

### 2.1 Test specimens

Residual stresses within two thermally exposed specimens with different substrate geometries (a flat specimen and an aerofoil-shaped specimen) were predicted using the FE method and were compared to corresponding experimentally measured values. The flat specimen has no ceramic TBC whereas the aerofoil specimen is coated with a full TBC system. In-plane residual stresses within the TGO of the flat specimen and those within the TBC of the curved one were derived and evaluated within the study. Dimensions, manufacturing parameters, coating compositions and details of heat treatments for each specimen are described below.

### 2.2 Manufacturing and ageing of specimens

The coated flat sample was supplied by Saeidi et al. and details of the parameters for the spraying process are presented in [29]. Nominal compositions for the substrate and the MCrAlY BC are listed in Table 1. The high velocity oxy-fuel (HVOF) process was used for spray deposition process of the coating, and MCrAlY powder size of 45±20μm supplied by Praxair (CO-210-24) was used as the feedstock. The sample was cooled by a compressed air jet during and after spraying. The thickness of the MCrAlY is ~300μm and it is applied to a substrate of approximate thickness 2mm. Two 8mm by 5mm strip specimens were cut and were heated isothermally within a furnace at 700°C or 1000°C for 96h then cooled in air.

The aerofoil-shaped specimen shown in Fig. 1 is made up of a CMSX4 substrate. The BC is Amdry 995 powder deposited by the HVOF deposition technique. Afterwards, air plasma sprayed (APS) 7 wt.% yttria stabilised zirconia TBC was applied. The compositions for the substrate and Amdry 995 powder are given in Table 2. The thicknesses of the BC and the TBC vary at different positions, P1 to P7 of the specimen and the values are listed in Table 3. Within the spallation experiments carried out by Seraffon et al. [26] the specimens were exposed to different temperatures, namely 900, 925, 950, 975 and 1000°C for varying times in laboratory air until failure occurred.

## 3. Model definitions

The build-up of radial stresses and hoop residual stresses in idealised coated substrates of various geometries are analysed using two different approaches. A simple analytical model is used to study the influence of global curvature (both concave and convex) upon the stresses in a simple single-layer coated system. An FE model is then used to examine the combined effects of global curvature and local roughness upon the stresses representative of a more practical system.

### 3.1. Analytical model

This model is based on existing published applications of thick cylinder theory [30]. It considers the influence of thermal expansion mismatch, elastic properties, curvature of the substrate and thickness of the coating on residual coating stresses. However, it neglects the effects of coating interface roughness, and of the creep and yield of the coatings. It also simplifies the problem by considering only a 'single-layer' coating on a homogeneous substrate, exploiting the facts that the elastic and thermo mechanical properties of the substrate and BC are broadly similar, and that the TGO is much thinner than the other layers of coatings. A system with internal and external coatings can be idealised as shown in Fig. 2. It is assumed that the ratio of the thickness of the substrate to that of the coatings is large; (10<ratio<1800).

At the interface of a solid convex component of substrate with radius $R_o$ and coating thickness $H$, the radial stress (which is the main driving force for opening of TBC discontinuities, leading to eventual spallation) can be expressed as shown in Eq (1). Similarly, the radial stress on the concave/inner surface of an infinite component of substrate radius $R_i$ is shown in Eq (2).

$$\sigma_r^{s,c}(r=R_o)=-\frac{E^c\left(\alpha^s-\alpha^c\right)\Delta T\left[\left(\frac{R_o+H}{R_o}\right)^2-1\right]}{1-2\nu^c+\left(\frac{R_o+H}{R_o}\right)^2+\frac{E^c}{E^s}\left(\frac{1+\nu^s}{1+\nu^c}\right)\left(1-2\nu^s\right)\left[\left(\frac{R_o+H}{R_o}\right)^2-1\right]} \quad (1)$$

$$\sigma_r^{s,c}(r=R_i)=\frac{E^c\left(\alpha^s-\alpha^c\right)\Delta T\left[1-\left(\frac{R_i-H}{R_i}\right)^2\right]}{1-2\nu^c+\left(\frac{R_i-H}{R_i}\right)^2+\frac{E^c}{E^s}\left(\frac{1+\nu^s}{1+\nu^c}\right)\left[1-\left(\frac{R_i-H}{R_i}\right)^2\right]} \quad (2)$$

where superscripts ‘s’ and ‘c’ represent substrate and coating, $E$ and $\nu$ are the elastic modulus and the Poisson’s ratio and α is the coefficient of thermal expansion (CTE).

The TBC system is assumed to be stress free at 925°C before the cooling takes place. The coating thickness is assumed to be 100μm. Fig. 3 shows the radial stresses at the coating interface for various systems with assumed elastic properties and CTEs of the substrate and the coating as given in Table 4 and a range of convex and concave curvatures. Stresses were evaluated using Eqs (1) and (2) for the system that has been cooled from a temperature of 925°C to 20°C.

As shown in Fig. 3, when the substrate becomes flatter, i.e. as $R_o$ or $R_i$ become large compared with $H$, the radial stresses caused by substrate curvature become insignificant. Significant changes in radial stresses occur only for radii smaller than 20mm. It is noteworthy that the profile of the coating surface contains local waviness profiles with radii of curvature which could be up to two orders of magnitude less than that of substrate’s overall geometry, and it is stresses from this local waviness which are likely to be dominant except at the most sharply-curved features of the substrate. Moreover, since the radial stresses arising from the concave curvatures are compressive, they tend to oppose those causing the TBC spallation, implying that such failure is more likely to occur on convex rather than concave surfaces. Similarly, hoop stress of the coating can be related to radius of curvature of the substrate. For the thin coating layer, the difference in hoop stresses across the coating thickness can be ignored. Hoop stresses values for different curvatures are plotted in Fig. 3. For both concave and convex curvatures, the coating hoop stresses are compressive and the magnitude increases as the substrate becomes flatter.

From Eqs (1) and (2), it can be seen that various factors other than substrate curvature (specifically, elastic properties) affect radial stresses at the coating interface. To examine the effects of these parameters relative to those of the substrate curvature, a simple sensitivity study was carried out. Elastic modulus (E), the Poisson ratio (ν) and the coating thickness were chosen for the study as variations in these parameters, during operation at high temperature, are significant. For example, E for the coating evolves due to densification/sintering with thermal exposure [31, 32] while changes in the composition due to inter-diffusion at the BC/substrate interface cause changes in the substrate properties. The calculated radial stresses and parameters for the study are normalised using the values at the reference point (R.P). Material parameters at the R.P are identical to the parameters from Table 4 except that the elastic modulus of the TBC is taken as 70GPa. Curvature and thickness of the TBC at the R.P are $0.154mm^{-1}$ and 300μm respectively. In comparison to curvature effects, interfacial radial stresses show significant sensitivity to coating parameters, especially the coating thickness and elastic modulus as shown in Fig. 4.

### 3.2. Finite element model

It is impractical to extend the analytical model to consider the combination of the macro-scale curvature and micro-scale roughness, so the FE techniques developed in [33] and [19] are used here, firstly to simulate residual stresses within the flat specimen without a TBC layer and with local coating roughness only, and then to study the interactions between coating roughness and substrate curvature in a TBC coated specimen.

The underlying modelling approach is similar in all cases, using appropriate periodic and symmetry boundary conditions to model a representative unit cell with a repeating pattern of the roughness at the TGO interfaces. The model takes account of composition changes within the BC and the influence on the creep and elastic properties of the BC [33], sintering of the TBC [19], if applicable, and formation of a thermally grown layer of alumina at the BC/substrate interface. As insufficient data could be found to parameterise an anisotropic oxide growth model, isotropic growth strain was applied to a layer of the BC within the FE model, with the value of strain being given by the Pilling-Bedworth ratio (PBR) of the aluminium-containing phases (β/γ’). A detailed procedure for implementation of those processes within a FE model, along with material properties of the TBC system, has been reported elsewhere [19].

The substrate used for the test specimens is CMSX-4 and the properties extracted from the literature are listed in Table 5. It was also assumed that the differences in weight percentage compositions between the substrate of the flat specimen and that of the aerofoil-shaped specimens are negligible, and properties from Table 5 were applied to both models. For every set of simulations, the TGO interface is assumed to be sinusoidal with amplitude and wavelength set to 6μm and 48μm, respectively. Dimensions of the model and a mesh diagram for the flat specimen are shown in Fig. 5 (i) and (ii). A generalised plane strain element was used because there is no axial restraint on the specimen as a whole, as shown in Fig. 5 (iii).

To represent an aerofoil shaped specimen, Fig. 1, with coated areas at both concave and convex curvatures, an FE model based on a hollow cylinder with internal and external coating as shown in Fig. 2 is used. The thicknesses of the BC and the TBC assumed for the model are 100μm and 200μm respectively. Additionally, to understand the effect of TBC thickness, a parametric study was conducted with different TBC thicknesses. The initial TGO thickness from the spraying process is assumed to be 1μm. It is assumed that the sinusoidal TGO interface is periodic along the axial direction as opposed to being periodic along the circumferential direction. With this assumption, an identical aspect ratio of the TGO interface can be used within the axisymmetric unit cell for both internal and external coating interfaces. A schematic diagram of the axisymmetric unit cell, mesh and boundary conditions for the model are shown in Fig. 6.

## 4. Results

### 4.1. Residual stresses within the TGO of the strip specimens as predicted by FE model

The model considers residual stresses within the TGO grown on the BC surface of the flat specimen at the end of cooling to 20°C after heating for 96h at 700°C or 1000°C. The predicted in-plane compressive residual stresses along the surface of the outermost TGO layers of two specimens are plotted in Fig. 7. For the specimen aged at 1000°C for 96h, the compressive stresses are predicted to cover the range between −1.0 and −3.0 GPa, while the corresponding values predicted for the 700°C specimen are higher, −2.6 to −3.4 GPa. Under both conditions, the residual in-plane stresses showed less compressive values at the peak of the TGO bump and changed monotonically to higher compression from peak to valley. Increase of the oxidation temperature from 700°C to 1000°C was found to signify this stress gradient change with curvature, Fig. 7.

### 4.2. Effects of curvature on stresses within the TBC system as predicted by FE model

Studies were carried out using models with different pairs of inner and outer radii of the substrate as shown in Table 6 to observe effects of curvature on hoop and radial stresses. Due to limitations in the availability of the diffusion model for evolution of the BC phases, and due to the lack of cyclic loading capability within the FE model, stresses are simulated for a specimen subjected to a single cycle of heat treatment from the experiment in [26], consisting of a 100h hold time at 925°C before cooling. At the end of steady state, tensile and compressive radial stresses are developed at the valley and the peak of the TGO/TBC interface due to oxide growth. These stresses will be superimposed onto the compressive thermal mismatch stresses created during cooling. Cooling-related changes of radial stresses at the valley of the TGO/TBC interface for different curvatures are illustrated in Fig. 8. Similarly, curvature has a significant effect on the radial mismatch stresses at the BC/TGO interface due to cooling although the interface is almost stress free during steady state due to creep of the BC [19]. Maximum tensile radial stresses at both TGO interfaces at the end of cooling for different curvatures are tabulated in Table 6.

Moreover, as suggested by the analytical model from Section 3.1, the influence of substrate curvature on hoop stresses at the TBC surface due to cooling can be observed from the FE model. The effect is illustrated in Fig. 9. The hoop stress of the TBC due to cooling is represented as the change in value of hoop stresses between the end of steady state and the end of cooling.

### 4.3. Effects of TBC thickness on stresses within the TBC system as predicted by FE model

It can be observed in a simple analytical model of a one-layer coating system that the thickness of the coating affects residual stresses within the coating (Fig. 4). To explore further the coating thickness effect in multi-layered systems, a parametric study was carried out using FE models with different TBC thicknesses. In contrast to the analytical calculations, the TBC thickness does not significantly affect either the TBC hoop or radial stresses at the TBC/TGO interface. However, an increase in TBC thickness causes a significant increase in radial stress at the BC/substrate interface, which has no local microscopic undulations. Therefore, it can be concluded that stresses at the TBC/TGO interface are dominated by local undulation and not the global coating thickness. The effects

of TBC thickness on the hoop and radial stresses within the TBC system are illustrated in Fig. 10.

### 4.4. Experimental results

Two piezospectroscopic stress analysis techniques, Raman spectroscopy (RS) and photo-stimulated luminescence piezo-spectroscopy (PLPS) have been used to measure residual stresses within the ceramic top coat and TGO layer of various TBC systems [12, 34-36]. The procedure and calibration for the Raman spectroscopy measurements are described in [37, 38]. The underlying mechanisms of the techniques differ but both methods measure the frequency shift of scattered or fluoresced light arising from the presence of a stress or strain in the material.

In this present work, the system used is a Renishaw Ramascope System 2000 spectrometer equipped with two laser sources: a He-Ne laser operating at a wavelength of 633 nm and maximum laser power of 25 mW; and an argon laser with a wavelength of 514 nm. For residual stress measurement in APS-TBC, the shifts of the Raman peaks are found to change linearly with hydrostatic stress. A conversion factor has been determined to be 5.60 $GPa^{-1}\cdot cm^{-1}$ by diamond anvil cell and the residual stress in the TBC measured by the Raman spectroscopy is considered to be a combined tri-axial state due to the large sampling volume of the incident laser. Specifically, a 1.5 μm incident laser beam on the surface of APS-TBC leads to a dispersed diameter of ~160 μm after passing through a thickness of ~180 μm and the sampling depth is ~40 μm [39], whereas the crystal size of YSZ is much smaller, being at the nano-metre scale [37], Hence the measured residual stress can be expressed by

$$\sigma_{hydro} = \Delta\nu_R/5.60 \tag{3}$$

where $\sigma_{hydro}$ is the hydrostatic stress and $\Delta\nu_R$ the shift of peak 640 $cm^{-1}$ from stress-free state in the Raman spectrum of tetragonal zirconia. Shifts toward higher frequency are associated with tensile stress. Due to the curvature of the TBC coated specimen, during the measurements a long working distance (LWD) Olympus objective, numerical aperture of 0.55, has been adopted, which gives a focus point with a diameter of ~1.5 μm to 2 μm.

The residual stress in the TGO was measured according to the shift of PLPS based on characteristic luminescence R1 and R2 lines (~693-694 nm) which originates from chromium ions ($Cr^{3+}$) in $Al_2O_3$. It was assumed that the residual stress in the thin TGO (~0.5 to 1.5 μm) is bi-axial and the stress component perpendicular to the surface is negligible. Hence a

conversion factor of 5.07 $GPa^{-1} \cdot cm^{-1}$ was adopted in this paper to convert the PLPS shifts to biaxial stress [40]:

$$\sigma_{bi-axial} = \Delta\nu_{PLPS}/5.07 \quad (4)$$

#### 4.4.1. Residual stresses within the TGO of the strip specimens as measured by PLPS

The stress measurements on the coating surface were made along paths which are parallel to the length and the width of the strip specimens, using a green laser (λ=514 nm) with spot diameter of approximately 1.5 μm. Twenty-one measurements were made for each path of the specimen at room temperature (20°C). The residual stresses within the TGO of the 700°C96h and 1000°C96h specimens are plotted in Fig. 11. The mean compressive stresses for the former and latter specimens are 1.06 GPa and 0.92 GPa with standard deviations (SD) of 0.45 GPa and 0.67 GPa respectively. The SD of the 1000°C96h specimen is much higher than the value for the 700°C96h specimen because of spikes caused by highly localised variations in TGO formation. The thickness of the TGO and the undulations of the TGO / BC were examined by SEM combined with "slice and view" using focused ion beam in a FEI Helios NanoLab 600i Dualbeam workstation. A trench created by *in situ* focussed ion beam milling is shown in Fig. 12 (i), which revealed the tortuous profile of the thin TGO layer formed on 1000°C96h specimen. In addition, the thickness of the TGO varies significantly from 0.2 μm to 1.5 μm. To understand non-uniformity in stresses across the TGO of the 1000°C specimen, two typical sites, a and b, selected from Fig. 12 (i) were investigated at a smaller scale as shown in Figs. 12 (ii) and 12 (iii) respectively. From these, the TGO grains are found to have varied sizes, directions and thicknesses. Additionally, the interfacial bonding between TGO and BC is expected to be location-dependent because of interfacial voids illustrated in Fig. **12** (iii). This in turn gives non-uniform residual stress distribution in the TGO of the 1000°C specimen (Fig. 11).

#### 4.4.2. Effects of curvature on stresses within the TBC system of aerofoil-shaped specimen as measured by Raman spectroscopy

After 100h of heating at 925°C, the aerofoil-shaped specimen was cooled and residual stress measurements undertaken using RS. Residual stresses within the as-sprayed specimen were also measured to examine the effects of manufacturing on initial residual stresses. Stress measurements were undertaken at a number of positions around the specimen giving

averaged stresses for a specific curvature. As shown in Fig. 13 for position P1, ten measurements were undertaken across the width of the specimen. The same procedure was adopted for other locations, Fig. 1, from P2 to P7. Stresses within as-sprayed and heat treated specimens are plotted against substrate curvature in Fig. 14. A considerable tensile residual stress, in the order of 1 GPa, results from the spraying-cooling of each splat and the cooling of the entire specimen to room temperature on the completion of the spraying process. In the as-coated condition, the lowest tensile residual stresses for both convex and concave curvatures are at the positions of the specimen (P6, P1 and P2) with the lowest curvature, Fig. 14. The trend of residual stresses vs curvature of heat treated specimen closely follows that of as sprayed specimen as demonstrated in Fig. 14.

## 5. Discussion

### 5.1. Comparison of residual stresses in the strip specimens

The measured stresses presented in Fig. 11 are smaller than the in-plane principal compressive stresses predicted by the FE models (Fig. 7), but of the same order of magnitude. The measured stresses for the 700°C96h specimen show similar mean stress with the 1000°C96h specimen compared with local highly compressive stresses embedded within less variable background data for the 1000°C96h specimen. Specifically, predicted values of compressive stresses within the 700°C96h specimen (2.0 to 3.5 GPa) are a factor of more than 2 larger than the range of experimental results (0.6 to 1.5 GPa) excluding outliers. Similarly, the predicted range of compressive stress for the 1000°C96h specimen of around 1.0 to 3.0 GPa is also around 2.5 times the range of the experimental results excluding the localised spikes (0.3 to 1.2 GPa).

One possible cause of discrepancy between predictions and experiment is the choice of oxidation law used for the FE model. This law is fundamental for calculating volume growth because of TGO formation and the corresponding growth stresses, and the phase balance within the inter-metallic coating. The law used in the present work is based on the empirical relationship derived from ref [41]. However, this relationship was obtained by extrapolating results from oxidation experiments [42] carried out at temperatures much higher than the range used for the present study. The model may therefore over-predict the oxide growth rate and in turn the levels of stress arising from oxide growth. Another possible reason is that in the FE model, the TGO is assumed to be completely bonded to the BC and the TBC. In reality, the bond is weakened by voids and cracks at the interface (Fig 12). Therefore, the completely bonded TGO within the model produces higher compressive stresses. A third

possible reason for differences relates to the way in which the oxidation results in stress build-up. The model assumes isotropic growth of the oxide layer. However, as discussed by Evans et al [43], oxide can grow via different mechanisms and the local distribution of TGO stress is dependent on the microstructure of the TGO. They proposed that TGO growth stress is highest if the new TGO grains are formed between two existing oxide grains, and stresses are lower for other situations of TGO grain formation. The model does not take account of microstructure nor of local variation in stresses arising from different growth mechanisms, so the effects of the actual growth mechanisms will not be represented in the results.

Another point of note is that, both for the experiment and the model, the 1000°C96h specimen shows a lower level of stress than the 700°C96h specimen, even though it would be expected that the greater thickness of TGO and the greater temperature difference on cooling in the former case would both lead to a higher level of stress. In terms of experimental results, it is apparent from the SEM and FIB analysis shown in Fig. 12 that interfacial bonding is more likely to be weakened by the formation of voids hence the residual stress applied by the constraint of the BC/substrate system is modified. The TGO layer is more convoluted than that in the 700°C96h specimen which can also be a factor in the relaxation of the laterally formed in-plane residual stress [44]. Moreover, creep of the BC and TGO at oxidation temperature can be a primary factor that relaxes the TGO layer and influences the TGO/BC bonding conditions during steady state [45, 46]. In the FEA modelling, the lower compressive residual stress in 1000°C96h specimen means that the residual stress generated by the faster growth of the TGO has been compensated by the creep relaxation of the BC at high temperature and the corresponding elastic modulus change with temperature during cooling, as given in Table 5.

### 5.2. Comparison of residual stresses in the aerofoil-shaped specimens

The separation of individual stress tensor components from the measurements of RS frequency shift is challenging because of random orientations of the grain structures within the sample volume, which determines the sensitivity of the shifts to each stress component [47]. An additional discrepancy from the FEA is that initial tensile residual stresses from spraying process as simulated in [48] were not coupled to the model for simplicity. To couple those residual stresses, additional FEA steps are required to simulate nonlinear time and temperature dependent spraying process and solidification process of molten coating particles. For the reasons explained earlier, quantitative comparison of measured values to predicted stresses is difficult. Therefore, only the trend of the dependency of reduction in in-

plane stresses at the TBC surface due to cooling on substrate curvature, as predicted by FE model, was compared against measured data.

Fig. 14 shows the residual stresses in the aerofoil-shaped specimen in the as-sprayed and thermally-exposed conditions. For the as-sprayed condition, there appears to be a weak dependency of residual stresses upon curvature though the trends are actually smaller than the scatter in the results and may therefore not be significant. By contrast, the stresses after thermal exposure show a stronger dependency upon curvature which is significant compared with the scatter. In order to understand how the experimentally-measured stresses illustrated in Fig. 14 may have arisen, and how they compare with the predictions, the following hypothesis is proposed.

1. When the coating is sprayed on to the specimen, it cools almost instantly and develops a high value of biaxial residual stress (quench stress). The stress distribution on cooling is as shown in line [i] on Fig. 14. The reasons for the apparent dependency of stresses upon curvature are not understood but if it exists at all it is relatively weak.
2. On re-heating to 925°C, the initial stress distribution from line [i] in Fig. 14 is superimposed onto a mismatch-related distribution for heating, which (by inverting Fig. 3 in order to give the trends relating to heating) adds slightly larger in-plane stresses for lower curvatures, tending to negate the weak trends apparent in line [i] in Fig. 14. The result is a stress distribution which is not precisely known but will be more tensile than the initial stresses and is shown diagrammatically as line [ii] in Fig. 14.
3. After exposure to 925°C for a period of time, creep stress relaxation results in a change of the distribution to be considerably less tensile as shown in line [iii] in Fig. 14. For simplicity it is assumed that the curvature-related variations in tensile stresses will be negligible by this stage, so the distribution is shown as being uniform.
4. On cooling back to room temperature again, the cooling-related thermal mismatch stress (which from Fig. 3 is seen to be more compressive for lower curvatures), is superimposed on the stress state from stage 3. The end result is an overall tensile distribution, but is less tensile for regions of lower curvature (line [iv] in Fig. 14)

The predictive FE model does not precisely model this situation because it does not take account of the process-induced initial (quench) stresses, but it does model the change in

stress which arises from cooling from 925°C to room temperature (Fig. 9). The trends agree well between the predicted stress change in Fig. 9 and the hypothesised change between the states shown in lines [iii] and [iv] of Fig. 14.

Although there are variations in TBC thickness at different positions of the aerofoil specimen, the sensitivity study using the FE model, for the range of thicknesses between 130 and 300μm, has shown that the changes in thickness do not significantly affect TBC hoop stresses. Therefore, it is reasonable to assume that fixing the TBC thickness for the FE models with different radii of curvatures will not introduces significant errors.

### 5.3. Relationship between substrate curvature and spallation or delamination failures

From the analytical model and FE studies on the effects of substrate curvatures, the direct relationship between the TGO interfacial stresses and the convex substrate curvatures can be observed. Meanwhile, an inverse relationship is observed for concave curvatures. Moreover, the radial interfacial stresses predicted for the convex coating are also higher than those for the concave coatings. These out-of-plane stresses play a major role in creating parallel cracks (cracks parallel to the TGO interface) within the TBC in the vicinity of the TGO interface and delamination cracks at the interfaces. Therefore, failure is expected at convex regions of the aerofoil specimens.

Flash thermography studies carried out by Seraffon et al. [26] on failed aerofoil specimens, which are similar to the one from Fig. 1, have also demonstrated that spallation of the coating is favoured at the convex regions of the specimen. Large scale delamination of TBC was observed at convex regions of the specimen that had been heated for 1050h at 1000°C. Conversely, spallation of coatings was not observed at the concave regions even after 1500h at 1000°C. These results give further confidence to the predictions made from the sensitivity study for the relationships among the TGO interfacial stresses, coating failure and substrate curvatures.

## 6. Conclusions

The present paper demonstrates the comparisons of residual stresses within the TGO and TBC predicted from two different FE models against experimental results obtained within the project consortium. Additionally, sensitivity of radial stresses on substrate curvature and predictions of coating spallation are also compared against experimental thermography

studies of coating spallation by project partners. These studies lead to the following conclusions:

- For the flat specimen, residual stresses are predicted to be of a similar order of magnitude to the stresses measured using the RS method. Both techniques demonstrated higher compressive residual stresses within the specimen that had been heated at the lower temperature of 700°C as opposed to 1000°C.
- For the aerofoil specimen, because of the slow relaxation of manufacturing-related tensile residual stresses (around 1GPa) within the aerofoil specimen at 925°C, TBC residual stresses after cooling are tensile rather than compressive as predicted by the FE model.
- An inverse relationship between substrate curvature and reduction in hoop stresses due to thermal mismatch predicted by FE model agrees with the trend given by the stresses from the RS method.
- From the analytical and FE models, it is expected that cracks will be initiated within the TBC and at the TGO interfaces for convex coatings rather than concave, especially at the regions with high curvatures. Failure of the TBC is favoured when there is coalescence of those cracks, and spallation of the TBC is therefore expected at the convex regions. This prediction is confirmed by flash thermography studies [26] of the aerofoil specimens after failure, for which the spallation/delamination of coating is observed at convex regions of the specimens.

There is mutual agreement in experimental results and FE predictions for the trend of dependence of residual stresses and TBC spallation on the global curvature as presented in this paper. This agreement demonstrates that various assumptions regarding to the geometry of the coating interfaces and the material properties within the FE models, are appropriate for predicting residual stresses and failure of the TBCs. However, quantitative comparison between the predicted residual stresses by the FE model and the experimental measurements is still found to be difficult.

**Acknowledgement**

We would like to acknowledge the support of The Energy Programme, which is a Research Councils UK cross council initiative led by EPSRC and contributed to by ESRC, NERC, BBSRC and STFC, and specifically the Supergen initiative (Grants GR / S86334 / 01 and EP / F029748) and the following companies; Alstom Power Ltd., Doosan Power, E.ON, National Physical Laboratory, Praxair Surface Technologies Ltd, QinetiQ, Rolls-Royce plc, RWE npower, Siemens Industrial Turbomachinery Ltd. and Tata Steel, for their valuable contributions to the project. We would also like to thank Prof. D. G. McCartney and Dr S. Saeidi (University of Nottingham) for providing the flat coated specimens.

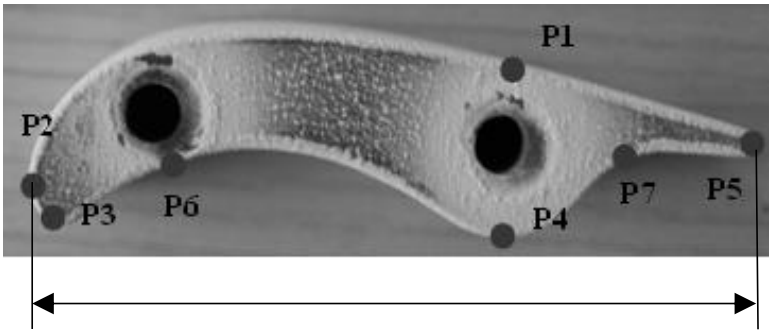


Fig. 1: A side view of the aerofoil shaped specimen coated with TBC showing measurement positions P1 to P7.

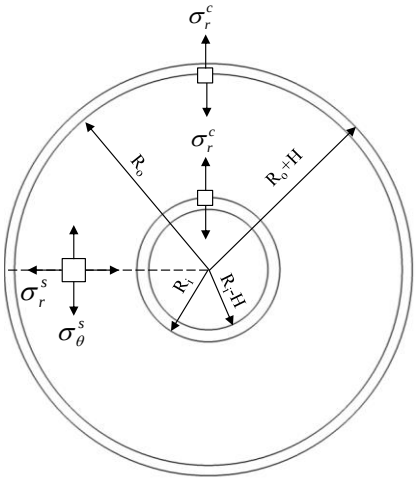


Fig. 2: Schematic diagram of a coating system with internal and external coatings, and illustration radial stresses at coating interface created by substrate curvature

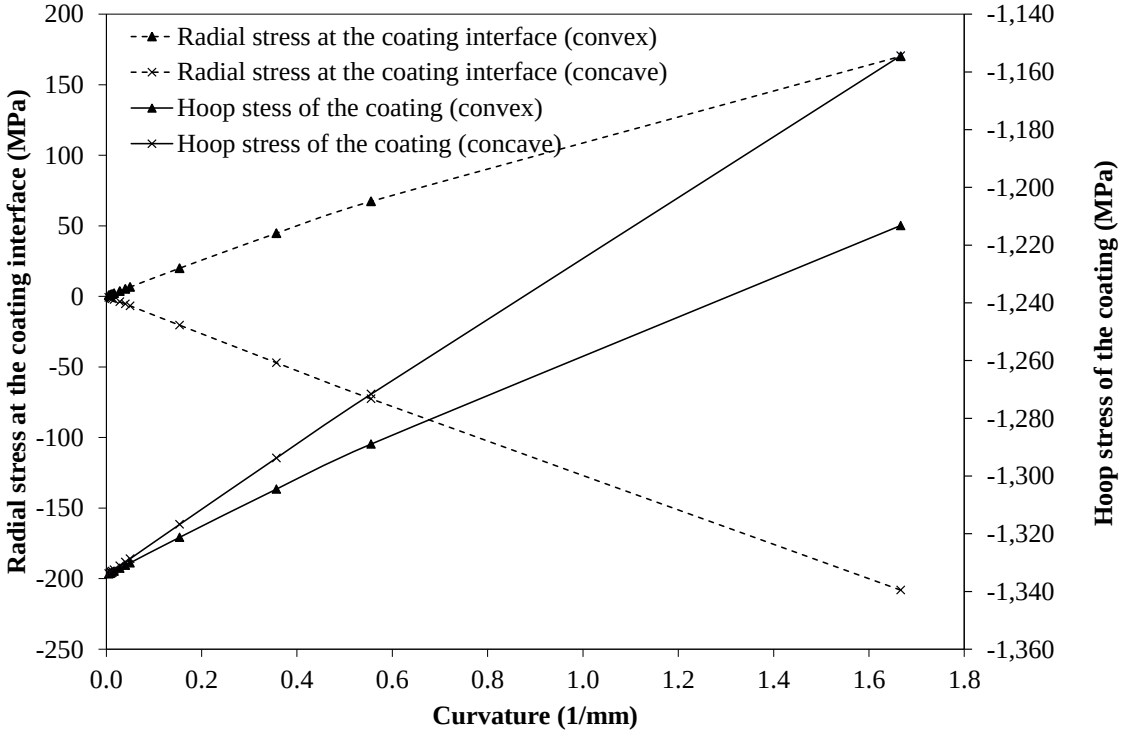


Fig. 3: Effect of curvature on the radial stresses at the concave and convex sides of the coatings at the end of cooling to 20°C from 925°C (Analytical model)

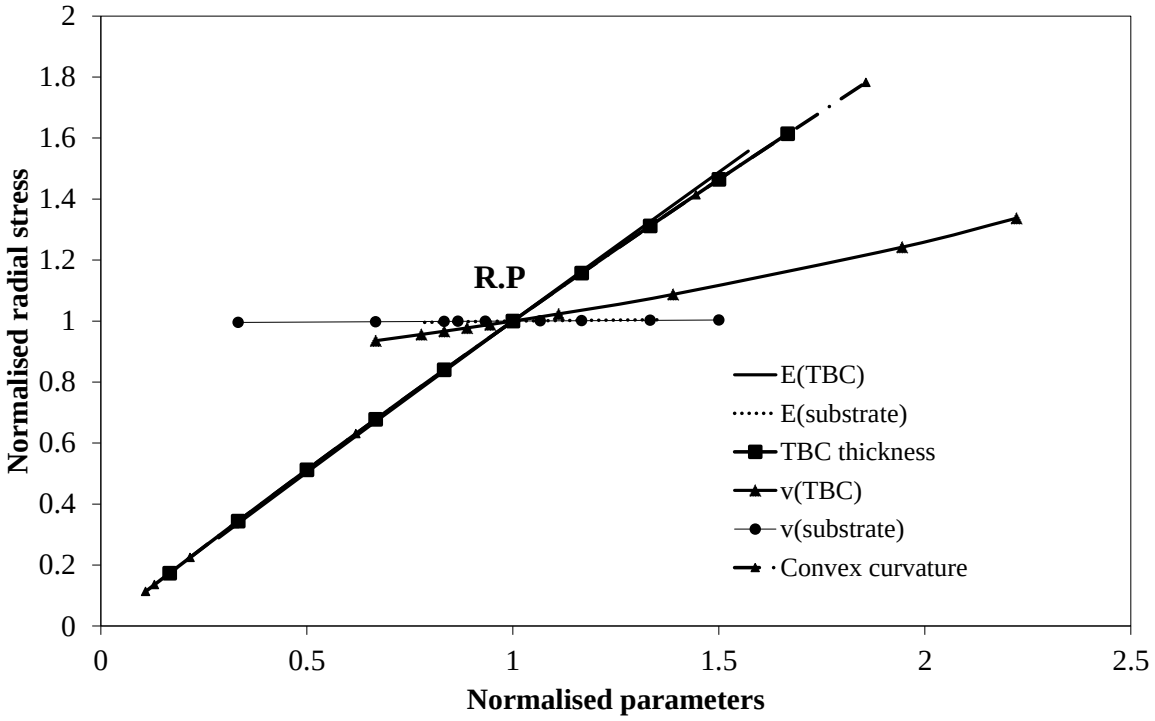


Fig. 4: Parametric study of the effects of input parameters on radial stresses at the coating interface using the analytical model [Eq (1)]

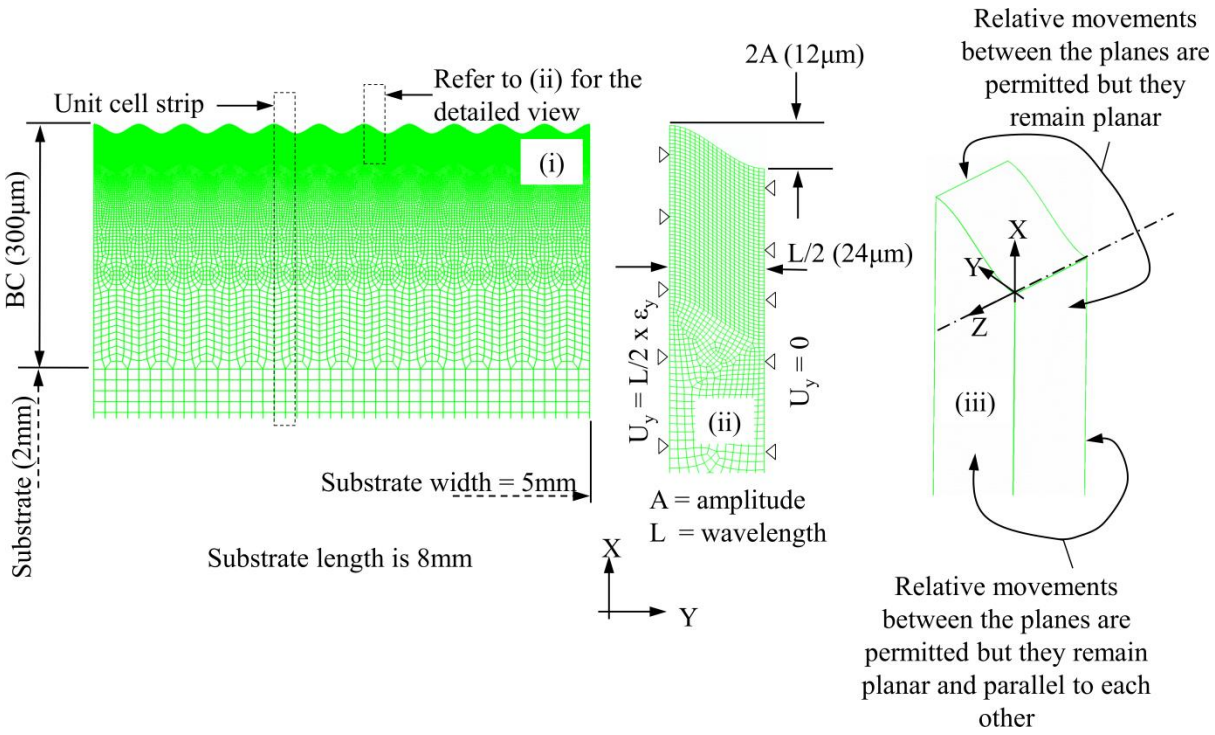


Fig. 5: (i) Dimension of the flat specimen and (ii) boundary conditions and detailed mesh diagram of the unit cell near the TGO; (iii) Physical interpretation of generalised plane strain boundary conditions

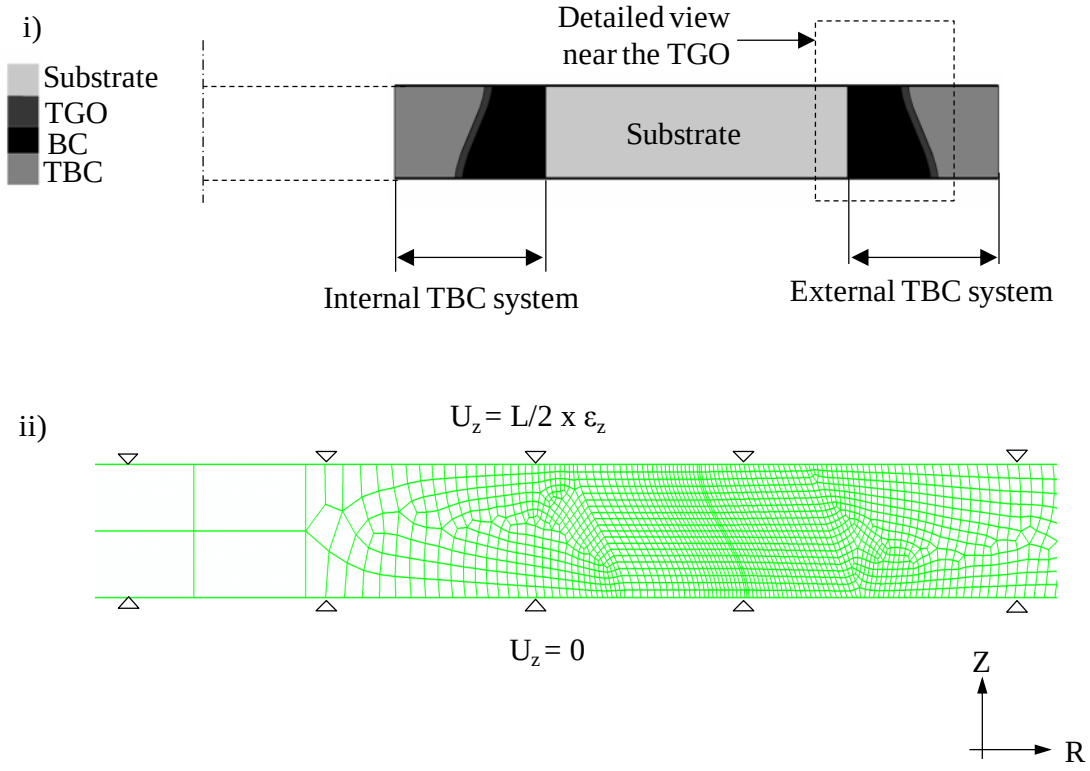


Fig. 6: (i) A schematic diagram of the unit cell to represent the hollow cylinder model from Fig. 2 and (ii) boundary conditions and detailed mesh diagram of the unit cell used near the TGO interface (R-Z axis represents the radial-axial coordinate system)

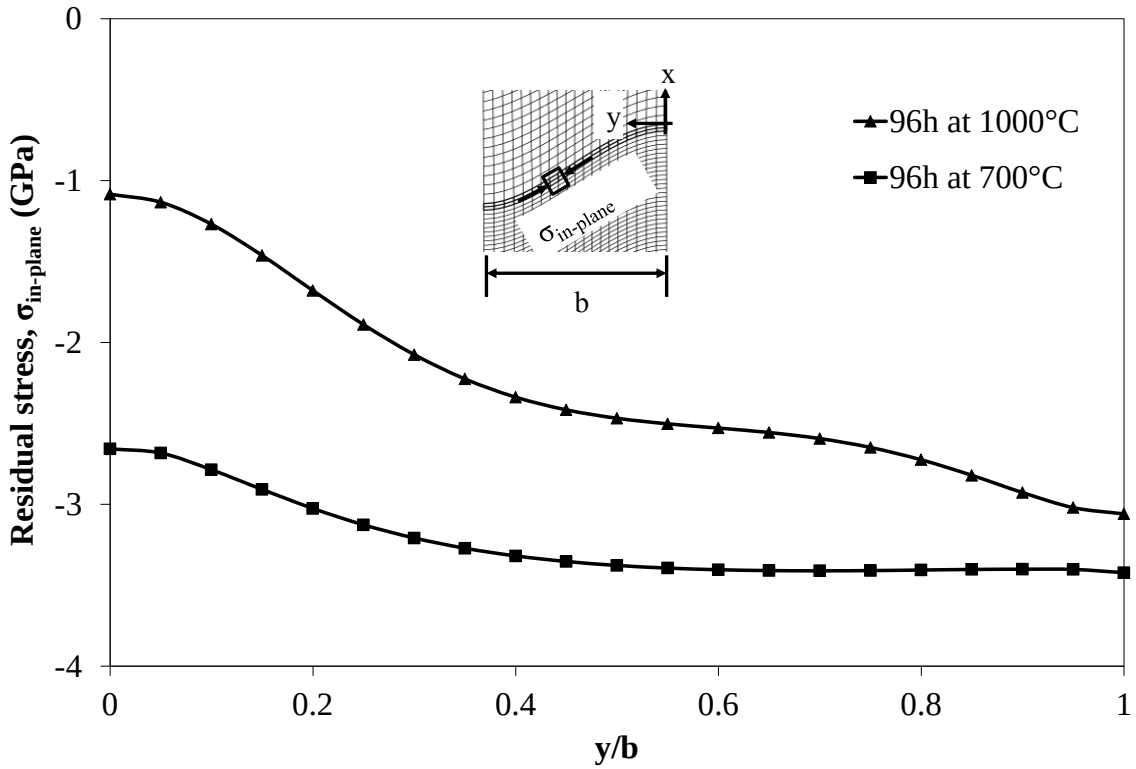


Fig. 7: In-plane compressive stress within a TGO at 20°C after oxidation at 1000°C and 700°C for 96h

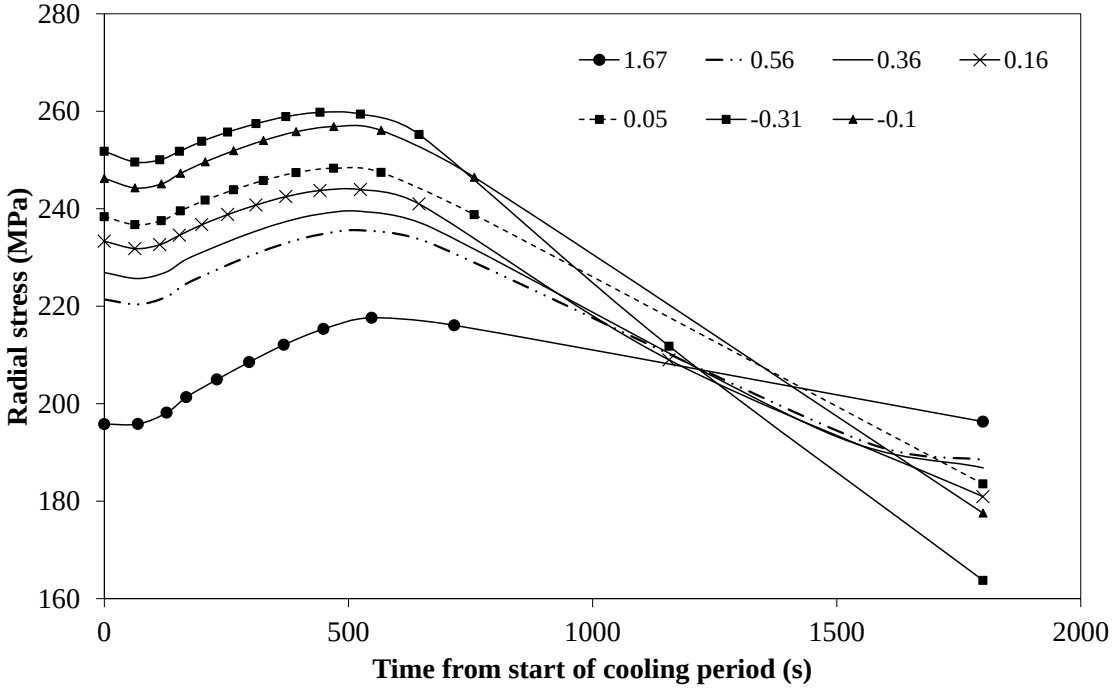


Fig. 8: Differences in evolution of radial stress at the valley of TBC/TGO interface, due to cooling after heating at 925°C for 100h, for different curvatures ($mm^{-1}$)

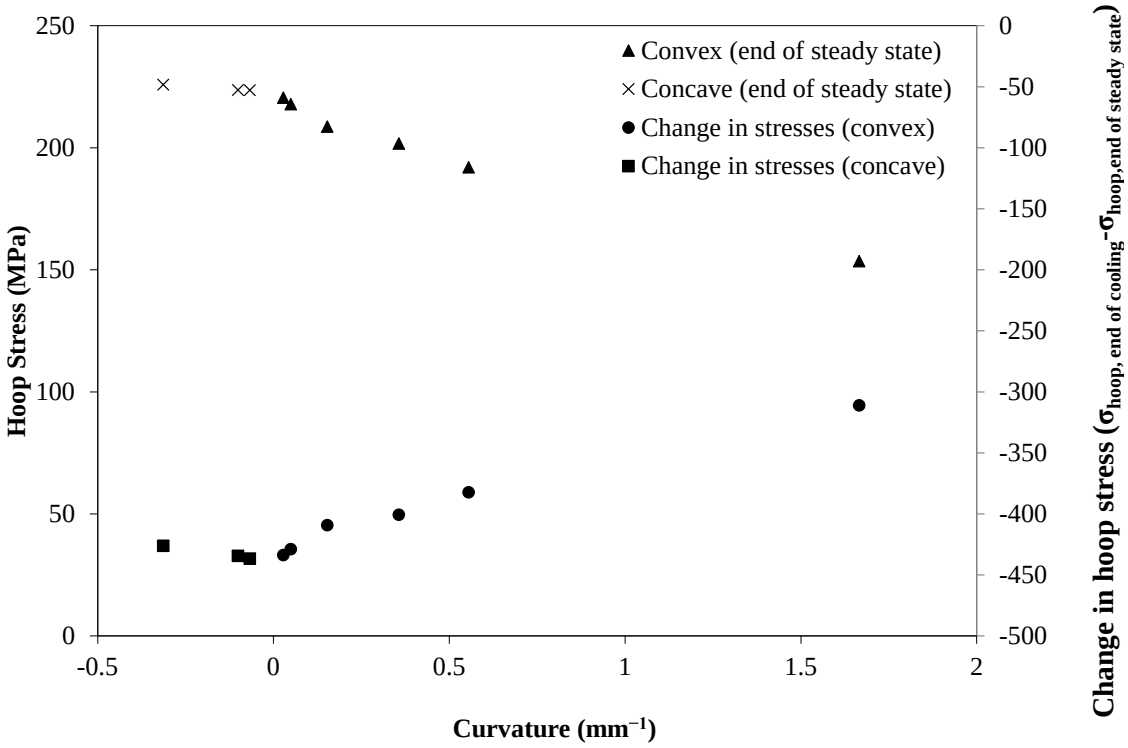


Fig. 9: Variations of hoop stresses of the TBC surface to substrate curvatures at the end of cooling after 100h at 925°C

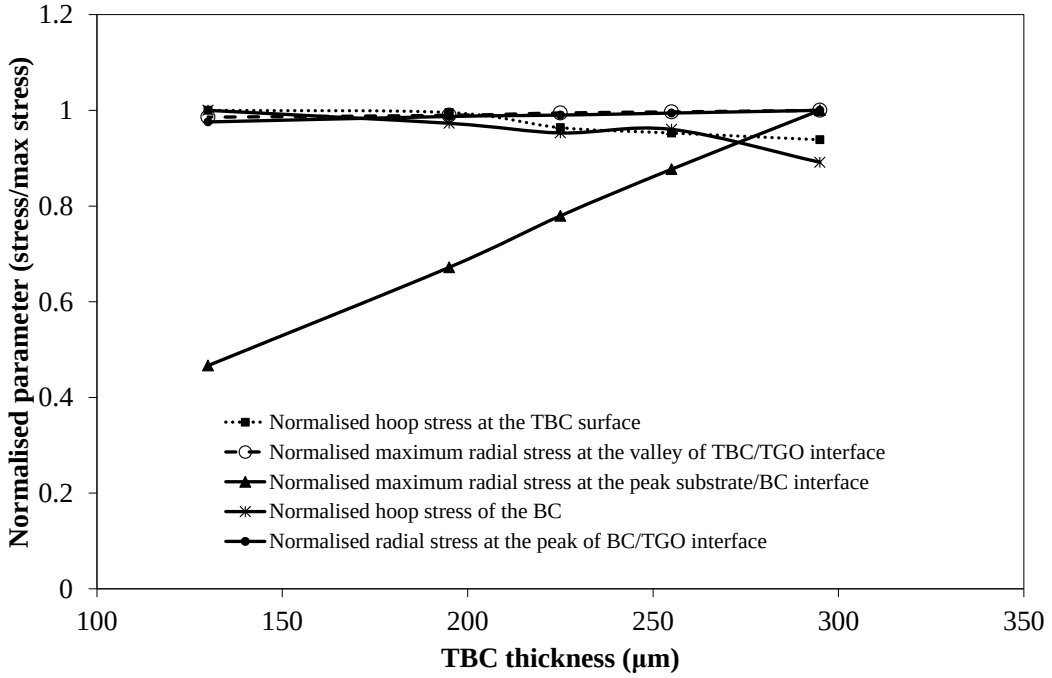


Fig. 10: Effects of TBC thickness on radial and hoop stresses within the TBC system (Stresses are at 20°C after heating for 100h at 925°C)

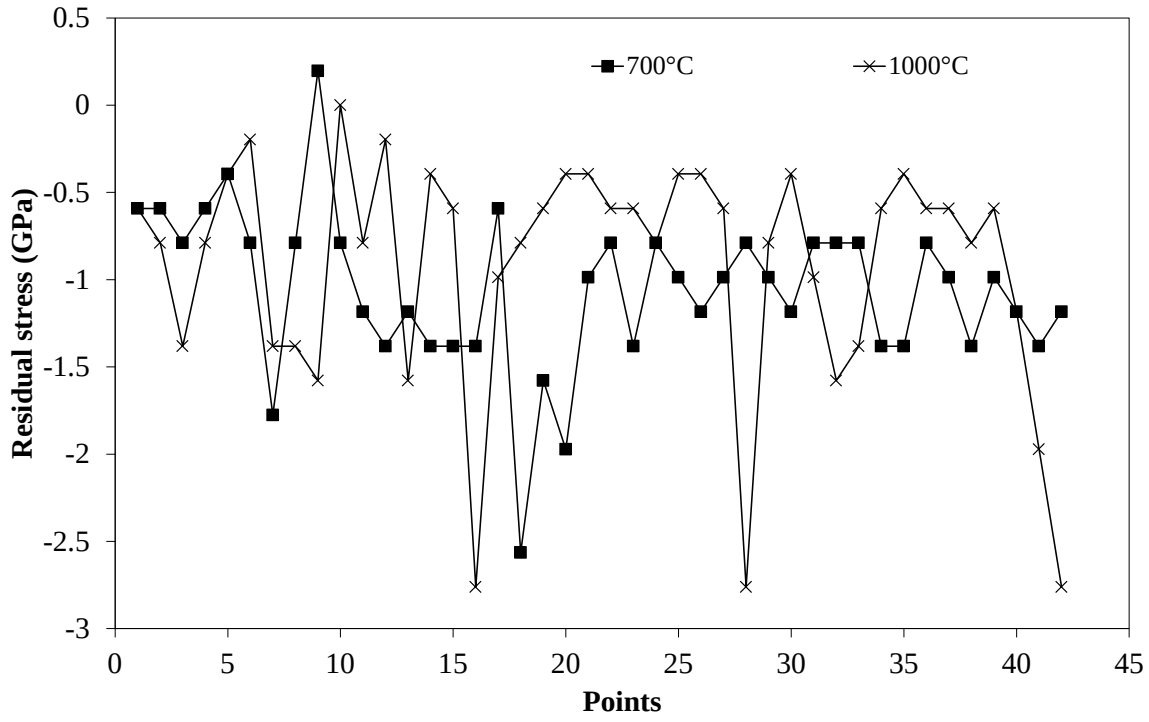


Fig. 11: Experimental residual stresses at the surface of the TGO at 20°C after oxidation at 1000°C and 700°C for 96h

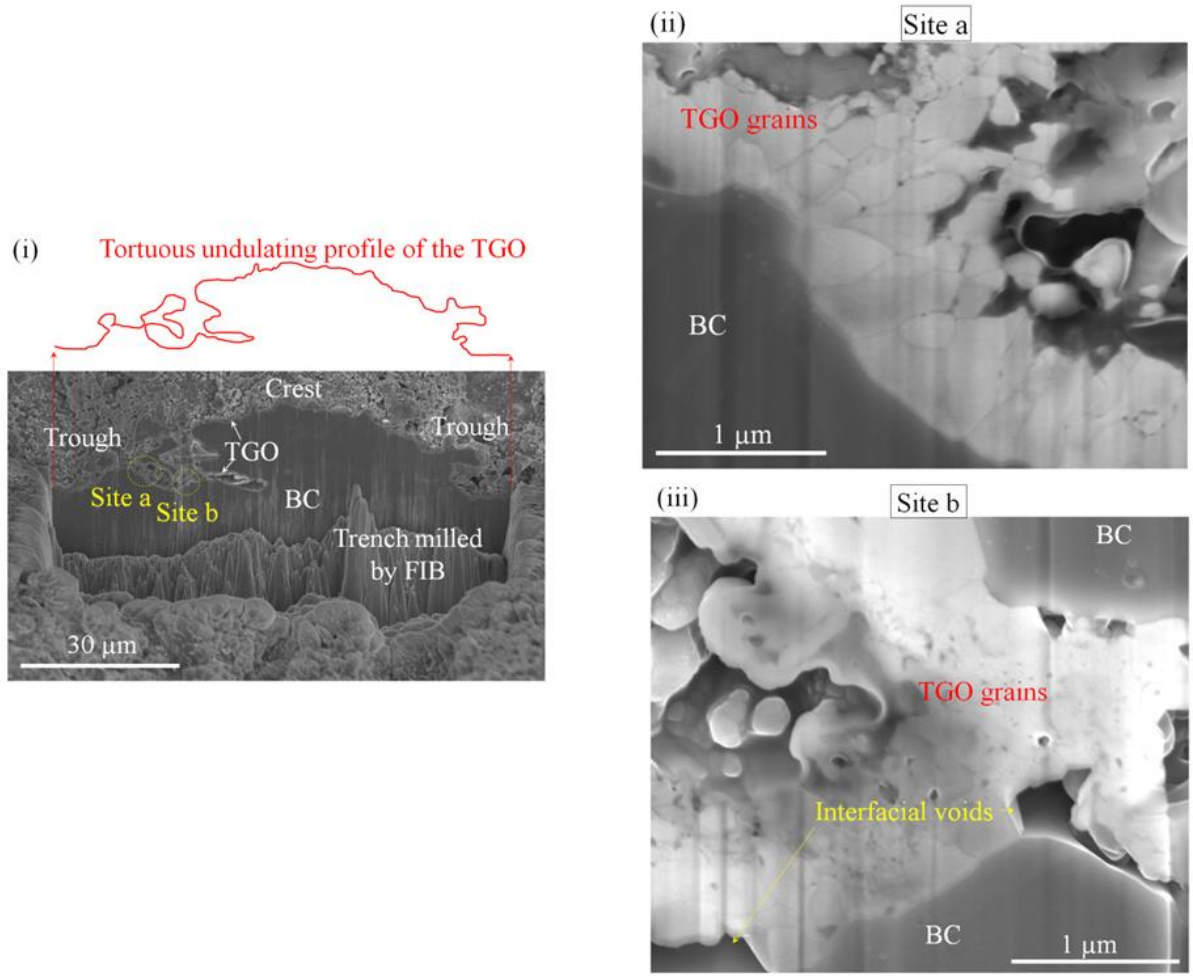


Fig. 12: SEM images showing (i) a typical cross-section, created by FIB milling, of an undulating bump consists of two troughs on the side of a crest. The surface layer is thin TGO with varied thickness, 0.2 to 1.5 µm, and it follows the torturous coating surface. Two sites, a and b, are shown in detail in (ii) demonstrating the varied sized and orientation of the TGO grains and (iii) the interfacial voids and non-uniformity of the TGO layer.

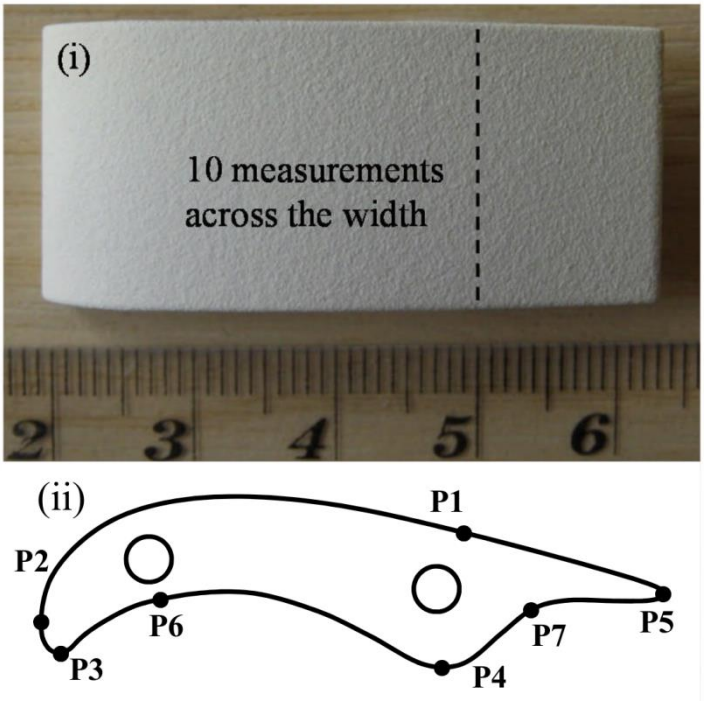


Fig. 13: (i) A top view of an aerofoil specimen showing the line at location P1, along which stress measurements were taken (ii) a side view of an aerofoil specimen.

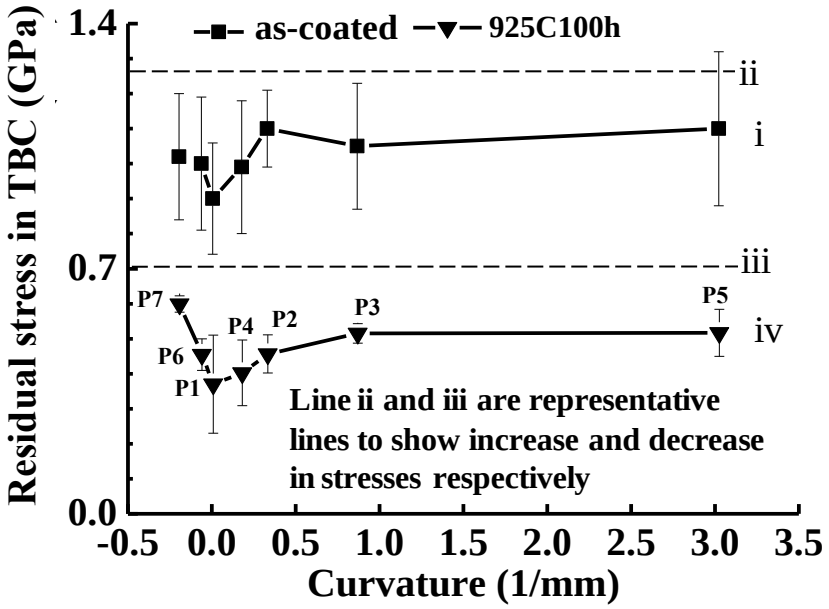


Fig. 14: Residual stress in the TBC changes with substrate curvature in as-coated and 925C100h specimens [49]

Table 1: Composition (in wt.%) of substrate and BC for the flat specimen

| **Alloy** | **Ni** | **Cr** | **Co** | **Al** | **W** | **Ti** | **Mo** | **Ta** | **Re** | **Hf** | **Y** |
|---|---|---|---|---|---|---|---|---|---|---|---|
| CMSX-4 | 58.99 | 6.46 | 9.61 | Base | 8.24 | 0.83 | 0.63 | 5.86 | 3.92 | - | - |
| AMDRY 995 | 32 | 21 | Base | 8 | - | - | - | - | - | - | 0.5 |

Table 2: Composition (in wt.%) of the substrate and BC for the aerofoil-shaped specimen

| **Alloy** | **Ni** | **Cr** | **Co** | **Al** | **W** | **Ti** | **Mo** | **Ta** | **Re** | **Hf** | **Y** |
|---|---|---|---|---|---|---|---|---|---|---|---|
| CMSX-4 | Base | 6.5 | 9.6 | 5.6 | 6.4 | 1 | 0.6 | 6.5 | 3 | 0.1 | |
| AMDRY 995 | 32 | 21 | Base | 8 | - | - | - | - | - | - | 0.5 |

Table 3: Coating thicknesses [50] and curvatures at the different positions, P1 to P7, of the specimen shown in Fig. 1 (Concave curvatures are denoted by a negative sign)

| **Position** | **P1** | **P2** | **P3** | **P4** | **P5** | **P6** | **P7** |
|---|---|---|---|---|---|---|---|
| **Curvature ($mm^{-1}$)** | 0.006 | 0.33 | 0.866 | 0.178 | 3.023 | -0.062 | -0.195 |
| **TBC thickness (μm)** | 220 | 190 | 190 | 210 | 130 | 220 | 250 |
| **BC thickness (μm)** | 110 | 50 | 90 | 100 | 50 | 130 | 135 |

Table 4: Elastic properties and CTEs of substrate and TBC for analytical stress calculations

| | Elastic modulus (GPa) | Poisson ratio | CTE ($10^6$ *$K^{-1}$) |
|---|---|---|---|
| Substrate | 140 | 0.3 | 20.7 |
| TBC | 113 | 0.18 | 10 |

Table 5: Material properties of CMSX-4

| Temperature (°C) | E [51] (GPa) | ν [51] | CTE [52] ($C^{-1}.10^6$) | $A_0$ [53] ($MPa^{-n}s^{-1}$) | Q [53] (J/mol) | n [53] |
|---|---|---|---|---|---|---|
| 200 | 155.0 | 0.3 | 15.0 | $6.68 \times 10^{48}$ | $1.72 \times 10^6$ | 6.6 |
| 630 | 134.0 | - | - | - | - | - |
| 830 | 120.0 | - | - | - | - | - |
| 1200 | 100.0 | - | - | - | - | - |

Table 6: Maximum radial stress at the TBC/TGO and at the BC/TGO interfaces at the end of cooling after 100h at 925°C

| Outer radius (mm) | Inner Radius (mm) | $\sigma_{radial}^{max}$ at the TBC/TGO interface; inner coating (MPa) | $\sigma_{radial}^{max}$ at the TBC/TGO interface; outer coating (MPa) | $\sigma_{radial}^{max}$ at the BC/TGO interface; inner coating (MPa) | $\sigma_{radial}^{max}$ at the BC/TGO interface; outer coating (MPa) |
|---|---|---|---|---|---|
| 0.6 | N/A | N/A | 200.4 | N/A | 719.4 |
| 1.8 | N/A | N/A | 193 | N/A | 672.5 |
| 2.8 | N/A | N/A | 190.7 | N/A | 661.1 |
| 6.2 | 3.20 | 154.38 | 180.9 | 603.95 | 648.8 |
| 20 | 10.00 | 177.54 | 183.58 | 620.87 | 641.92 |
| 35 | 15.00 | 180.75 | 183.6 | 625.73 | 639.6 |

**References**


[1] R.A. Miller, J. Am. Ceram. Soc., 67 (1984) 517–521.
[2] J.W. Fairbanks, R.J. Hecht, Mater. Sci. Eng., 88 (1987) 321-330.
[3] S.M. Meier, D.K. Gupta, K.D. Sheffler, "Ceramic Thermal Barrier Coatings for Commercial Gas Turbine Engines" (Overview), (March 1991) pp. 50-53.
[4] R.A. Miller, Surf. Coat. Tech., 30 (1987) 1-11.
[5] S. Bose, High temperature coatings, Elsevier Butterworth-Heinemann, 2007.
[6] A.G. Evans, D.R. Mumm, J.W. Hutchinson, G.H. Meier, F.S. Pettit, Prog. Mater. Sci., 46 (2001) 505-553.
[7] D.S. Rickerby, M.R. Winstone, Mater. Manuf. Process., 7 (1992) 495-526.
[8] M. Ahrens, R. Vaßen, D. Stöver, S. Lampenscherf, J. Therm. Spray. Tech., 13 (2004) 432-442.
[9] D.S. Rickerby, G. Eckold, K.T. Scott, I.M. Buckley-Golder, Thin. Solid. Films., 154 (1987) 125-141.
[10] R.T. Wu, X. Wang, A. Atkinson, Acta. Mater., 58 (2010) 5578-5585.
[11] V.K. Tolpygo, D.R. Clarke, K.S. Murphy, Surf. Coat. Tech., 188-189 (2004) 62-70.
[12] R.J. Christensen, D.M. Lipkin, D.R. Clarke, K. Murphy, Appl. Phys. Lett., 69 (1996) 3754-3756.
[13] T. Tomimatsu, S. Zhu, Y. Kagawa, Acta Mater., 51 (2003) 2397-2405.

[14] P. Fauchais, G. Montavon, G. Bertrand, J. Therm. Spray. Techn., 19 (2010) 56-80.
[15] V. Teixeira, M. Andritschky, W. Fischer, H.P. Buchkremer, D. Stöver, Surf. Coat. Tech., 120-121 (1999) 103-111.
[16] M. Martena, D. Botto, P. Fino, S. Sabbadini, M.M. Gola, C. Badini, Eng. Fail. Anal., 13 (2006) 409-426.
[17] H.E. Evans, M.P. Taylor, J of Corros sci & eng, Vol 6 (2003).
[18] K. Chan, S. Cheruvu, R. Viswanathan, Proceedings of ASME Turbo Expo, Atlanta paper number GT2003-38171, (2003).
[19] S.T. Kyaw, I.A. Jones, T.H. Hyde, Eng. Fail. Anal., 27 (2013) 150-164.
[20] M. Ranjbar-Far, J. Absi, G. Mariaux, F. Dubois, Mater. & Des., 31 (2010) 772-781.
[21] J.W. Hutchinson, J. Mech. Phys. Solids., 49 (2001) 1847-1864.
[22] E.P. Busso, H.E. Evans, Z.Q. Qian, M.P. Taylor, Acta Materialia, 58 (2010) 1242-1251.
[23] E.P. Busso, J. Lin, S. Sakurai, M. Nakayama, Acta Mater., 49 (2001) 1515-1528.
[24] U. Hermosilla, M.S.A. Karunaratne, I.A. Jones, T.H. Hyde, R.C. Thomson, Mater. Sci. Eng. A, 513-514 (2009) 302-310.
[25] D. Liu, P.E. Flewitt, K.R. Hallam, Key Eng. Maters., 9-12 (2012).
[26] M. Seraffon, N.J. Simms, J.R. Nicholls, J. Sumner, J. Nunn, Mater. High Temp., 28 (2011 ) 309-314.
[27] Dong Liu, Peter EJ Flewitt, O. Lord, Conf. Engineering Structural Integrity Assessment: From plant and structure design, maintenance to disposal (Manchester Conference Centre, Manchester, UK), (24 - 25 May 2011).
[28] D. Liu, M. Seraffon, P.E.J. Flewitt, N.J. Simms, J.R. Nicholls, D.S. Rickerby, J. Eur. Ceram. Soc., 33 (2013) 3345–3357.
[29] S. Saeidi, K.T. Voisey, D.G. McCartney, J. Therm. Spray Technol., Volume 18 (2009) 209-216.
[30] X.Y.Gong, D.R.Clarke, Oxid. Met. , 50 (1998) 355-376.
[31] C.F. B. Siebert, R. Vaβen, D. Stöver, , J. Mater. Process. Tech., 92-93 (1999) 217-223.
[32] J.A. Thompson, T.W. Clyne, Acta Materialia, 49 (2001) 1565-1575.
[33] U. Hermosilla, University of Nottingham, (Thesis (PhD), 2008).
[34] A. Selcuk, A. Atkinson, Maters. Sci. & Eng. A, 335 (2002) 147-156.
[35] Y. Sohn, K. Schlichting, K. Vaidyanathan, M. Gell, E. Jordan, Metall. & Maters. Trans. A, 31 (2000) 2388-2391.
[36] V. Teixeira, M. Andritschky, W. Fischer, H.P. Buchkremer, D. Stöver, J of Maters. Process. Tech., 92–93 (1999) 209-216.
[37] Dong Liu, Oliver Lord, P.E.J. Flewitt, Appl Spectrosc, 66 (2012 Oct ) Pg 1204-1209.
[38] D. Liu., University of Bristol, (Thesis (PhD), 2012).
[39] D. Liu, O. Lord, O. Stevens, P.E.J. Flewitt, Acta Materialia, (2012).
[40] Q. Ma, D.R. Clarke, J. Am.Ceram. Soc., 76, ((1993)) 1433-1440.
[41] M.S.A. Karunaratne, S.L. Ogden, S.D. Kenny, R.C. Thomson, Maters. Sci. & Tech., Volume 25 (2009) 287-299.
[42] S.M. Meier, D.M. Nissley, K.D. Sheffler, Phase II Final Report,Technical Report NASA Contractor Report 18911/NAS3-23944,National Aeronautics and Space Administration, NASA LewisResearch Cente, (1991).
[43] A.G. Evans, J.W. Hutchinson, Int. J. Solids. Struct., 20 (1984) 455-466.
[44] D.R. Clarke, Acta. Mater., 51 (2003) 1393-1407.
[45] A.M. Huntz, G.C. Amiri, H.E. Evans, G. Cailletaud, Oxid. Met., 57 (2002) 499-521.
[46] Y.C. Zhou, T. Hashida, Int. J of Solids and Struct., 38 (2001) 4235-4264.
[47] A. Atkinson, S.C. Jain, J. Raman. Spectrosc., 30 (1999) 885-891.
[48] D.Y. Ju, M. Nishida, T. Hanabusa, J MATER PROCESS TECH, 92–93 (1999) 243-250.
[49] D. Liu, P.E. Flewitt, K.R. Hallam, Oxid. Met., (2013, in press.).
[50] M. Seraffon, PhD thesis (The University of Cranfield), (2012).
[51] H. Takagi, M. Fujiwara, K. Kakehi, Maters. Sci. & Eng. A (2004) 348-351.
[52] K. Mills, Woodhead Publishing, (2002 ).
[53] D. Woodford, CORROSION, April 3 - 7, 2005 , Houston, Tx, (2005).